Temperature Dependence of Two Key Interstellar Reactions of H_3^+: $O(^3P) + H_3^+$ and $CO + H_3^+$

Stephen J. Klippenstein* and Yuri Georgievskii

Chemical Sciences and Engineering Division, Argonne, National Laboratory Argonne, Illinois 60439

Benjamin J. McCall

Department of Chemistry and Department of Astronomy, University of Illinois, Urbana−Champaign, Urbana, Illinois 61801

The reactions of H_3^+ with CO and with $O(^3P)$ are the two most important reactions for the destruction of H_3^+ in dense interstellar clouds. These two reactions are studied with sophisticated theoretical methods that should provide accurate predictions for the rate coefficients. The potential energy surfaces are studied with high-level electronic structure methods. For both reactions, simple long-range expansions are shown to be sufficiently accurate for predicting the kinetics at room temperature and lower. The kinetics is predicted from a combination of transition state theory, trajectory simulations, and master equation analysis. For the $O(^3P)$ reaction, the interplay between the spin−orbit and the charge−quadrupole interactions is explicitly considered. For the CO reaction, we also consider the isomerization and decomposition dynamics of the two initially formed adducts. The final predictions, which are expected to be accurate to about 10 to 20%, are compared with the available experimental data. For the $O(^3P)$ reaction, the predicted rate coefficient is accurately reproduced by the expression $1.14 \times 10^{-9} (T/300)^{-0.156} \exp(-1.41/T)$ cm^3 molecule^{-1} s^{-1} over the 5 to 400 K temperature range. For the CO reaction, the predicted rate coefficients for the $H_2 + HCO^+$ and $H_2 + HOC^+$ channels are accurately reproduced by the expressions $1.36 \times 10^{-9} (T/300)^{-0.142} \exp(3.41/T)$ and $8.49 \times 10^{-10} (T/300)^{0.0661} \exp(-5.21/T)$ cm^3 molecule^{-1} s^{-1}, respectively, over the 10 to 400 K temperature range. These revised rate coefficient expressions imply an increase in the destruction of H_3^+ at temperatures that are typical of dense clouds (10−30 K) by a factor of 2.5 to 3.0.

Introduction

Since its first detection in interstellar clouds in 1996,[1] the H_3^+ molecular ion has proven to be a powerful probe of interstellar conditions. In recent years, considerable attention has been devoted to the diagnostic role of H_3^+ in diffuse interstellar clouds, where it is produced by cosmic-ray ionization and destroyed by dissociative recombination with electrons. The unexpectedly high abundance of H_3^+ observed in diffuse clouds[2,3] generated some controversy, as it was unclear whether the adopted value of the ionization rate was too low or that of the dissociative recombination rate coefficient was too high. A series of storage ring experiments[4,5] and theoretical calculations[6,7] finally fixed the low-temperature value of the recombination rate, and thereby established that the cosmic-ray ionization rate in diffuse clouds is roughly an order of magnitude higher than previously thought.[4,8,9] This high ionization rate (which cannot be directly measured near Earth because of the influence of the solar wind) may be an indication of a previously unrecognized large flux of low-energy cosmic rays.[10]

Comparatively less attention has been paid to H_3^+ in dense star-forming regions, where it plays the key role in initiating a network of ion−molecule reactions that lead to the formation of many of the ~150 known interstellar molecules.[11] Since the initial work of Geballe and Oka,[1] there have been many subsequent detections of H_3^+ in such clouds.[12−14] All of these detections have been interpreted using a very simple model of

the H_3^+ chemistry, wherein formation by cosmic rays is balanced in steady state by destruction by proton transfer reactions. Considering the impact of the recent clarification of the H_3^+ destruction rate in diffuse clouds (by dissociative recombination), we decided to re-examine the two dominant destruction pathways for H_3^+ in dense clouds, which are the title reactions.

In earlier analyses of dense cloud H_3^+ (e.g., McCall et al.[2]), the reaction with CO was considered to be the dominant destruction pathway, because of its large roughly Langevin rate coefficient of 1.7×10^{-9} cm^3 molecule^{-1} s^{-1}.[15] This reaction is responsible for the production of HCO^+, which has been a widely used tracer of dense cloud material since its initial detection as the unidentified "X-ogen" line in 1970.[16] The reaction with atomic O, which according to astrochemical models[17] has a number density roughly equal to that of CO, has long been thought to be slower, with a rate coefficient of 8×10^{-10} cm^3 molecule^{-1} s^{-1},[18] and was therefore taken to be negligible. However, it should be noted that a more recent experiment has increased this value to 1.2×10^{-9} cm^3 molecule^{-1} s^{-1}.[19] This reaction initiates the production of interstellar water and is therefore quite a critical one from an astrochemical perspective. These two reactions have furthermore been identified in sensitivity analyses[20] as among the most important ones in terms of the impact of their current uncertainties on chemical abundances in interstellar clouds.

In the present paper, we perform state of the art calculations using dynamically corrected transition state theory (TST) to obtain the temperature-dependent rate coefficients of both of

---

* Corresponding author.

T Dependence of Two Key Interstellar Reactions

J. Phys. Chem. A, Vol. 114, No. 1, 2010 **279**

these key destruction reactions for H_3^+. For the O + H_3^+ reaction, this work builds on the earlier trajectory study of Collins and co-workers[21] by including a detailed treatment of the effect of the spin−orbit interaction on the charge−quadrupole interaction. Our treatment of this effect is closely analogous to that of Gentry and Giese.[22] The importance of this coupling was nicely illustrated in a study of Herbst and co-workers on the related reaction of C(^{3}P) with H_3^+.[23] We also employ a more accurate potential energy surface than Collins and co-workers for the O + H_3^+ reaction. Recent theoretical work on CO + H_3^+ has focused on ab initio evaluations of the stationary points on the potential energy surface.[24,25] Here, we focus on a detailed analysis of the overall kinetics including a careful treatment of the different terms in the potential and the branching between the H_2 + HCO^+ and the H_2 + HOC^+ channels. Earlier theoretical work also considered this rate coefficient and branching ratio but with more limited representations of the potential.[26]

The present calculations reveal that, at the low temperatures of dense clouds, the rate of the H_3^+ + O reaction is roughly equal to the value previously assumed for H_3^+ + CO (and generally taken as the entire destruction rate of H_3^+). Furthermore, the H_3^+ + CO reaction is about 50% faster than previously thought and produces both HCO^+ and HOC^+ efficiently. The cumulative result of these rate coefficient increases is that H_3^+ is destroyed ~2.5 times faster in dense clouds than previously thought. As discussed below, this implies either that the lines of sight through dense clouds are ~2.5 times longer than previously thought or that the cosmic-ray ionization rate is ~2.5 times higher than expected. Furthermore, the production of interstellar H_2O and HOC^+ must be faster than assumed by current astrochemical models.

Theory

Overview. For both reactions, a classical treatment of the rate coefficient for capture provides a useful starting point for the analysis. We have recently derived a version of transition state theory (TST) that is particularly appropriate for predicting this rate coefficient for capture at moderately low temperatures, for example, 10−100 K.[27] This long-range TST emphasizes the role of different terms in the long-range asymptotic potential form and builds on the large body of theory developed for predicting long-range capture rate coefficients.[28] It can be viewed as a limiting case of our variable reaction coordinate TST approach,[29,30] with the latter providing accurate estimates for much higher temperature via the incorporation of accurate interaction energies and the explicit consideration of angular momentum conservation.

For an asymptotic expansion of the long-range interaction potential with $V \propto R^{-n}$ (where R is the distance between the centers-of-mass of the two reactants), the capture rate coefficient may be expressed as[28]

$$k = C_1 \mu^{-1/2} V_0^{2/n} T^{1/2-2/n} \qquad (1)$$

where μ is the reduced mass of the system, V_0 specifies the strength of the interaction, and T is the temperature (in energy units). The constant C_1 depends on the form of the interaction and the rotational dimension of the system but is independent of μ, V_0, T, and the reactant moments of inertia. It is determined from simple classical phase space integrals. Explicit C_1 values are provided in ref 27 for a variety of common interactions.

For multiple terms in the long-range expansion, the simple analytic form of eq 1 no longer holds, but results are readily obtained via numerical integration of low dimension phase space integrals. Furthermore, these numerical integrations are simple enough to incorporate direct determinations of the interaction potential via ab initio quantum chemical simulations. Here, we implement and compare analytic long-range potential based results and direct ab initio potential based results employing a variety of electronic structure methodologies. For the ab initio potential based results, we employ our direct variable reaction coordinate-TST approach.[31,32] We also employ rigid-body trajectory simulations of the capture process for long-range representations of the potential to examine the deviations from statistical predictions for both the overall rate coefficient and the product branching. These trajectory simulations are performed as described in refs 33 and 34.

For both reactions, there are a number of further complications that must be considered in predicting the overall rate coefficient. In particular, for the O(^{3}P) reaction, there are multiple electronic states, and the coupling of the spin and orbital angular momenta to each other and to the charge−quadrupole interaction lead to significant deviations from the classical results.[22,23] For the CO reaction, there are two distinct binding orientations, leading to different products via two distinct ion−molecule complexes. Furthermore, these two ion−molecule complexes are kinetically coupled via a transition state that lies below the energy of the reactants. Thus, it is important to consider the branching both in the initial formation of these complexes and in their subsequent decay to bimolecular products.

O(^{3}P) + H_3^+ Reaction. The charge−quadrupole interaction is generally the longest ranged interaction between an atom and an ion.[35] Ignoring for the moment any spin−orbit interactions, the operator for this charge−quadrupole interaction is given by (Appendix A)

$$\hat{V} = \frac{3Qq}{2l(2l-1)R^3}\left(\hat{L}_z^2 - \frac{1}{3}\hat{L}^2\right) \qquad (2)$$

where Q is the quadrupole moment of the atom, q is the electronic charge of the ion, and $\hat{L}^2$ and $\hat{L}_z$ are the operators for the square of the electronic orbital angular momentum of the atom and its projection on the axis connecting the ion and the atom, which without loss of generality is assumed to be parallel to the z axis. For O(^{3}P), the electronic orbital angular momentum $l = 1$; so, the eigenvalue for $\hat{L}^2$ is $l(l + 1) = 2$, and the eigenvalues for $\hat{L}_z$ are $m_l = 0, \pm1$. The eigenvalues for $\hat{V}$ in eq 2 then reduce to

$$V = -\frac{Qq}{R^3} \quad m_l = 0$$
$$= \frac{Qq}{2R^3} \quad m_l = \pm1 \qquad (3)$$

This long-range potential is contrasted with that obtained from explicit CASPT2 (second order multireference perturbation theory employing a complete active space wave function)[36] ab initio simulations in Figure 1. The CASPT2 calculations employed a six electron six orbital (6e,6o) active space consisting of the three valence orbitals of H_3^+ and the three p orbitals of the O atom. They employ a complete basis set estimate (CBS)[37−39] based on results for the augmented triple (aug-cc-pVTZ) and augmented quadruple-ζ (aug-cc-pVQZ)
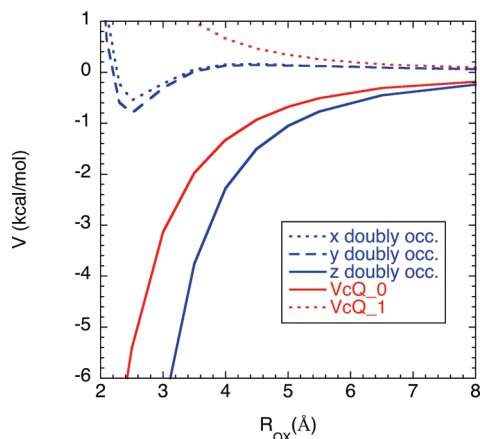
Figure 1. Plot of the potential energy for O(^{3}P) interacting with H_3^+ as a function of the distance R_{OX} between the O atom and the center of mass of H_3^+. The blue lines correspond to the CASPT2(6e,6o)/CBS results for the three distinct orientations of the doubly occupied p orbital of the O atom. The z axis is the internuclear OH axis, while the x axis is the out-of-plane axis. The two red lines correspond to the charge−quadrupole potentials for $m_l = 0$ (solid) and $m_l = \pm1$ (dotted).

Figure 2. Plot of the calculated capture rate coefficient for H_3^+ + O(^{3}P) employing (i) the directly sampled CASPT2(4e,3o)/CBS ab initio potential (solid), (ii) the charge−quadrupole potential (Charge-Q; dotted), (iii) the charge−induced-dipole potential (Charge-Ind. Dip.; dashed), and (iv) the sum of the charge−quadrupole and charge−induced-dipole potentials (Charge-Q + Charge-Ind. Dip.; dashed-dotted).

correlation-consistent polarized-valence basis sets of Dunning.[40,41] These ab initio interaction energies are expected to be highly accurate. The quadrupole moment (0.91 au = 1.22 D Å) for the analytic potential (eq 3) is obtained from related CASPT2-(4e,3o)/aug-cc-pVQZ evaluations for the O atom. Calculations with the (4e,3o) active space are essentially identical to those for the (6e,6o) active space. Furthermore, calculations with multireference configuration interaction or coupled cluster methods such as QCISD(T) (quadratic configuration interaction with singles, doubles, and perturbative treatment of connected triples)[42] also yield very similar potential energy curves. All of the ab initio electronic structure calculations reported here were performed with the MOLPRO package.[43]

As predicted by eq 3, at long-range there are two repulsive surfaces correlating with $m_l = \pm1$ and one attractive surface correlating with $m_l = 0$. (Note that each of these three electronic surfaces has a spin degeneracy of 3 to yield the total of 9 spin−orbit states). The long-range charge−quadrupole interaction is essentially identical to the ab initio interactions down to about 7 Å. Then, as the separation decreases further, the analytic charge−quadrupole and the ab initio surfaces are increasingly divergent, with the ab initio potentials all being lower. Although not shown in Figure 1, the next most important term in the expansion involves the ion induced dipole term, which is proportional to $1/R^4$. The polarizability of the O atom is 0.77 Å^3 = 5.2 bohr^3.[44] At short-range, the attractive surface correlates with the doubly occupied O atom p orbital pointing toward the H_3^+ center-of-mass. The two excited state surfaces, which correlate with the two other orientations for the doubly occupied O atom p orbital, are weakly attractive near R_{OX} = 3 Å and then become repulsive again at 2.2 Å.

In the following analysis, we shall assume that the electronic motions are adiabatic, with no dynamical transitions between the different electronic states. This assumption seems appropriate given the long-range nature of the relevant dynamics at low temperature. With this electronically adiabatic assumption, the two excited electronic states, with $m_l = \pm1$, do not contribute to the association rate coefficient because of their repulsive nature at short range. Their long-range repulsive nature also suggests that the opposite limit of rapid electronic crossings to yield a statistical distribution of states would predict similar rate coefficients.
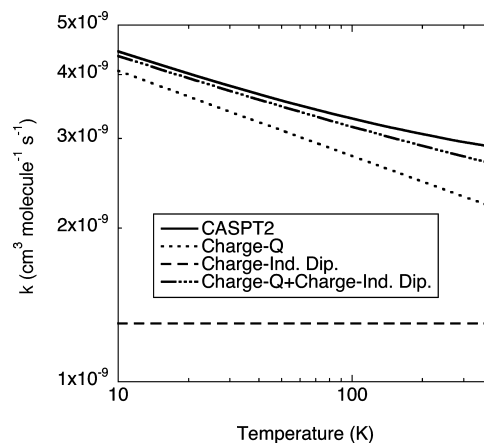
The isotropic nature of the long-range charge−atomic-quadrupole interaction implies that the capture rate coefficient for the ground electronic state is given by eq 55 of ref 27.[35] This expression reduces to

$$
\begin{aligned}
k(T) &= \sqrt{8\pi}(^1/_2)^{2/3}\Gamma(^1/_3)\mu^{-1/2}(Qq)^{2/3}T^{-1/6} \\
&= 8.46\mu^{-1/2}(Qq)^{2/3}T^{-1/6}
\end{aligned}
\tag{4}
$$

In Figure 2, this analytic expression for the capture rate coefficient is contrasted with that obtained from numerical integration of the partition function employing direct CASPT2-(4e,3o)/CBS ab initio evaluations of the interaction energy for the ground electronic state. A third calculation employed the sum of the charge−quadrupole interaction and the charge−induced-dipole interaction. Each of these calculations ignores the effect of spin−orbit interactions. The CBS extrapolation is obtained from the average of extrapolations for the cc-pVDZ, cc-pVTZ and aug-cc-pVDZ, aug-cc-pVTZ basis set pairs.

The analytic charge−quadrupole and direct CASPT2 based rate coefficients gradually approach one another as the temperature is lowered. At 10 K, they differ by about 10%, whereas at 400 K they differ by about 25%. Including the charge−induced-dipole interaction, which is the next term in the long-range expansion, greatly decreases the discrepancy, with the difference at 400 K now being only 8%. Note that the rate coefficients for the sum potential is not simply the sum of those for the individual components but instead is determined by the dynamics on the full potential. In general, the capture rate coefficient for a sum of potential terms is lower than the simple sum of the component rate coefficients.

These predictions of the rate coefficient for capture on the electronic ground state must be corrected for the effect of the electronic orbital and spin degeneracies. The three electronic states for the charge−quadrupole interaction correlate with the three choices for the spatial orientation of the doubly occupied p orbital in the O atom. The triple spin degeneracy for each of these orbital states then yields an overall degeneracy of nine. However, the spin−orbit interaction splits these states to yield the $^3P_2$, $^3P_1$, and $^3P_0$ states at energies of 0, 159, and 227 cm^{-1} and with degeneracies of 5, 3, and 1, respectively.

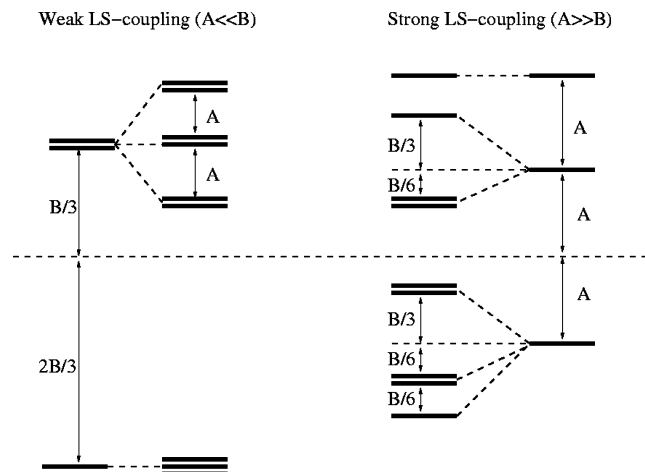Weak LS−coupling (A<<B)   Strong LS−coupling (A>>B)

Figure 3. Schematic diagram of the strong and weak LS-coupling limits for the charge−quadrupole interaction of eq 6.

The electronically adiabatic assumption now implies that two components of the $^3P_2$ state, all three components of the $^3P_1$ state, and the singly degenerate $^3P_0$ state will be nonreactive. Then, if we continue to ignore the effect of the spin−orbit interaction on the charge−quadrupole interaction, the rate coefficient in eq 4 should be corrected by the factor $3/q_{electronic}$, where $q_{electronic}$ is the electronic partition function given by

$$q_{electronic} = 5 + 3\exp[-E(^3P_1)/k_BT] + \exp[-E(^3P_0)/k_BT]$$
(5)

There are two limiting cases for the effect of the spin−orbit interaction on the charge−quadrupole interaction. A schematic diagram illustrating the two limiting cases of weak and strong spin−orbit interactions is provided in Figure 3. When the spin−orbit coupling is small relative to the charge−quadrupole interaction, the role of the spin−orbit interaction is simply to provide a degeneracy for the electronic states as outlined above. This limit is appropriate at high temperatures where the transition state lies at short separations with a relatively large charge−quadrupole interaction.

When the spin−orbit interaction is not small relative to the charge−quadrupole interaction, the ion−atom interaction energy can be obtained via the diagonalization of the full electronic Hamiltonian of the system, which includes both of these interactions,

$$\hat{V} = B\left(\hat{L}_z^2 - \frac{1}{3}\hat{L}^2\right) - A\hat{S}\cdot\hat{L}$$
(6)

where $B = 3Qq/(2R^3l(2l-1))$ defines the strength of the charge−quadrupole interaction and A is the spin−orbit coupling constant.

The second limiting case is that of large A (relative to B), for which the diagonalization approximately yields for the three lowest levels, (Appendix B)

$$E_0 = -\frac{B}{3} - A$$
$$E_{1,2} = -\frac{B}{6} - A$$
(7)

The complete set of nine levels is illustrated in Figure 3. However, here, we are interested in only the three lowest levels because the remaining six levels correlate with the upper two triply degenerate ab initio surfaces. As illustrated in Figure 1, these upper states are repulsive at short-range and so do not contribute to the addition kinetics.

This large A limit is appropriate at low temperatures where the transition state lies at large separation R, and B is thus small. Furthermore, note that in the rate coefficient evaluations these curves can be shifted up by A, which is independent of R and is the large R limit of each of the E_0, E_1, and E_2. The potential for the lowest level, E_0 is then 1/2 as attractive as that in eq 3, while that for the next lowest level is 1/4 as attractive and is doubly degenerate. Thus, the overall rate coefficient in this limit is equal to that from eq 4 times $[(1/2)^{2/3} + 2(1/4)^{2/3}]/3$ (= 0.474) times the $3/q_{electronic}$ correction factor. That is, in the low temperature limit, the effect of the coupling of the spin−orbit and charge−quadrupole interactions is to decrease the rate coefficient by about a factor of 2. When combined with the $3/q_{electronic}$ factor, the overall reduction of the rate coefficient for capture in the low temperature limit is by a factor of 3.5.

As the temperature increases, the transition state moves to closer separation and B increases and must ultimately become larger than A. Thus, to treat a broad range of temperatures, one must diagonalize the expression for the charge−atomic-quadrupole interaction energy (eq 6), which yields the following expressions for E_0, E_1, and E_2 (Appendix B)

$$E_0 = -\sqrt{\frac{(B+A)^2}{4} + 2A^2} - \frac{B}{6} + \frac{A}{2}$$
$$E_{1,2} = -\sqrt{\frac{B^2}{4} + A^2} - \frac{B}{6}$$
(8)

Now, the rate coefficient can be evaluated by employing these two expressions for the potential (again after shifting by A) in the long-range transition state theory formalism. The overall rate coefficient is then given as

$$k = (k_0 + 2k_1)/q_{electronic}$$
(9)

where k_0 and k_1 are the rate coefficients for reaction on the E_0 and E_1 potentials, respectively.

For large A, the expressions in eq 8 reduce to those in eq 7. For small A, the expressions in eq 8 reduce to

$$E_0 = -\frac{2B}{3} - \frac{2A^2}{B}$$
$$E_{1,2} = -\frac{2B}{3} - \frac{A^2}{B}$$
(10)

For $A = 0$, these potentials are degenerate and are equal to the $m_l = 0$ case of eq 2, thereby recovering the low A rate coefficient of eq 4.

The calculated rate coefficient for capture is illustrated in Figure 4 for the full diagonalization (intermediate A case) as well as for the two limiting cases. These calculations consider only the charge−quadrupole interaction. Interestingly, the intermediate A case switches between the small and the large A cases in precisely the temperature range of interest here. The midpoint of the transition occurs at about 70 K, where the thermal energy and the spin−orbit interaction are roughly
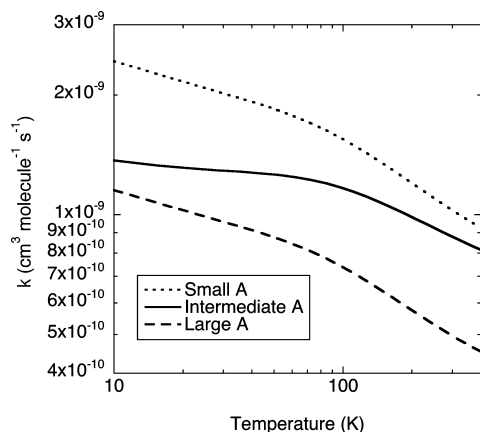
Figure 4. Plot of the calculated capture rate coefficient for $H_3^+ + O(^3P)$ with the full diagonalization (intermediate A case) and with the two limiting cases of large or small spin−orbit interaction A.

equivalent. The change in the slope of the curves at about 80 K is due to the increasing magnitude of the electronic partition function for the O atom.

The intermediate A case, charge−quadrupole capture rate coefficient prediction should still be corrected for the effects of the higher order terms in the potential as illustrated in Figure 2. As noted above, the predominant correction term involves the charge−induced-dipole interaction. The proper treatment of these corrections would involve the diagonalization of the interactions in the full spin−orbit space, as was done for the charge−quadrupole interaction. However, in this case, the predominant components are independent of spin−orbit state, and so we choose to ignore the spin−orbit induced corrections. Notably, the treatment of Gentry and Giese considers the effect of the anisotropy in the polarizabity.[22] Their results suggest that our neglect of the anisotropy in the charge−induded-dipole interaction will introduce errors of no more than a few percent. The final calculation thus involves the calculation of the capture rate coefficients k_0' and k_1' for the potentials

$$E_0' = E_{CASPT2/CBS} + E_0 + 2B/3$$
$$E_1' = E_{CASPT2/CBS} + E_1 + 2B/3 \qquad (11)$$

where E_0 and E_1 are from eq 8. The final rate coefficient is given by the analogue of eq 9.

The rate coefficients for capture on these potentials were evaluated with both long-range TST and trajectory simulations. The trajectory predictions were identical to the TST predictions, demonstrating that there is no recrossing of the TS surfaces for this reaction because of the isotropic nature of the potential.

CO + H_3^+ Reaction. The CO molecule has a small nonzero dipole moment, d, of 0.043 au (0.110 D),[45] with the C atom slightly negative and the O atom slightly positive. Thus, the charge−dipole interaction

$$V_{cd} = -\frac{dq}{R^2} \cos \theta \qquad (12)$$

is the longest ranged term for the interaction of CO with H_3^+. However, in the transition state region for the temperatures of interest here (i.e., for separations on the order of 20 au), the charge−quadrupole

$$V_{cQ} = \frac{Qq}{4R^3}(3 \cos^2 \theta - 1) \qquad (13)$$

and charge−induced-dipole interactions

$$V_{cid} = -\frac{q^2(\alpha_\parallel \cos^2 \theta + \alpha_\perp \sin^2 \theta)}{2R^4} \qquad (14)$$

are of comparable magnitude to the charge−dipole interaction because of the much larger values for the CO quadrupole moment ($Q = -2.92$ au $= -3.92$ D Å)[46] and polarizability components ($\alpha_\parallel = 15.7$ au $= 2.32$ Å^3 and $\alpha = 12.1$ au $= 1.79$ Å^3).[47]

These three terms in the potential are illustrated in Figure 5 for the linear approach of H_3^+ to the C atom in CO. The dominance of the charge−dipole term at large R implies that it is the dominant factor in determining the rate coefficient for capture in the low temperature limit. But the crossover between the charge−quadrupole and the charge−dipole interactions occurs at the large separation of 15 Å. Thus, the charge−quadrupole interaction becomes important already at rather low temperature. Although the charge−induced-dipole interaction is quite small here, this interaction is still of importance to the capture kinetics because it is attractive for all orientations, whereas the charge−dipole and charge−quadrupole interactions are both repulsive for some orientations.

The orientation dependence of the sum potential, $V_{cd} + V_{cQ} + V_{cid}$, is illustrated in Figure 6, with plots for addition to the C side ($\theta = 0$), to the O side ($\theta = 180°$), and perpendicular to CO ($\theta = 90°$). Notably, the charge−quadrupole term is the same for addition to either the C side or the O side of CO, while the charge−induced-dipole term has only a weak orientation dependence. Thus, at least at long-range, the difference in binding to the two sides arises primarily from the charge−dipole term. Correspondingly, the charge−dipole interaction plays a key role in determining the branching between $H_3^+...CO$ and $H_3^+...OC$ in the addition process. Meanwhile, for the perpendicular attack the long-range interaction is repulsive because the charge−quadrupole term is repulsive, while the charge−dipole term is zero.

The small magnitude of the dipole moment creates some difficulty for ab initio based evaluations of the interaction energy. For example, at the MP2 (second order Moller−Plesset perturbation theory) level, the dipole moment is predicted to be 0.097 au for the CBS limit or about 2.3 times too large. The QCISD(T) approach provides a much more accurate prediction for this dipole moment. Indeed, a CBS extrapolation of the predicted CO dipole moment based on explicit cc-pVDZ and cc-pVTZ calculations (at the aug-cc-pVQZ geometry) yields a CO dipole moment of 0.052 au, or only 20% larger than the experimental value for the ground rovibrational state (and only 10% larger than the experimental value of 0.048 au for the equilibrium geometry[45]). This QCISD(T)/CBS approach provides a similarly accurate prediction for the quadrupole moment of −2.90 au.

We have used this QCISD(T)/CBS approach to test the importance of additional terms in the potential beyond the three long-range terms of eqs 12−14. The plot in Figure 6 demonstrates that the three term long-range expansion is accurate down to separations of 7−8 Å (at 7 Å the discrepancy is only 20%).[48] The calculated capture rate coefficients for the three individual terms in the potential, for the sum potential, and for a directly evaluated QCISD(T)/CBS potential are illustrated in Figure 7.
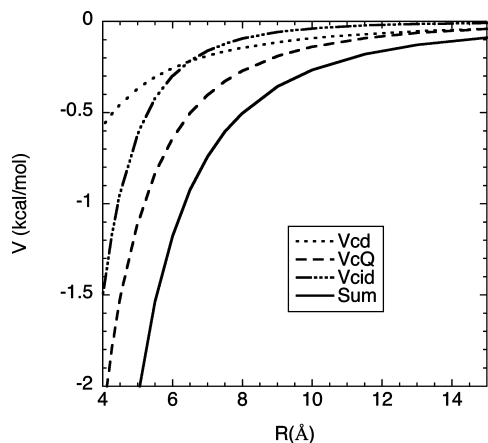
T Dependence of Two Key Interstellar Reactions

J. Phys. Chem. A, Vol. 114, No. 1, 2010 **283**

Figure 5. Plot of the potential energy for the linear addition of H_3^+ to the C side of CO. The dotted, dashed, and dash-dot lines denote the charge−dipole, charge−quadrupole, and charge−induced-dipole interactions, respectively. The solid line denotes the sum of these three interactions.
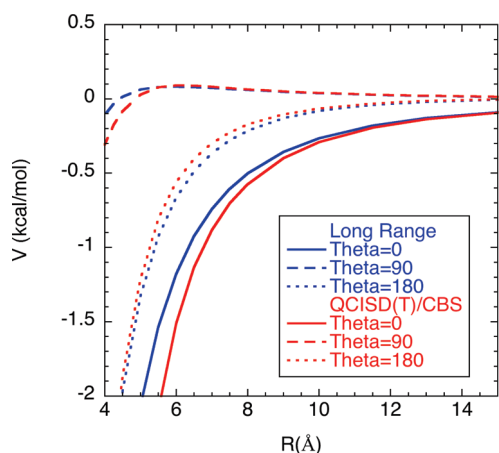

Figure 6. Plot of the interaction energy for the addition of H_3^+ to CO at angles of 0 (linear addition to the C side of CO), 90° (addition perpendicular to the CO axis through the CO center-of-mass), and 180° (linear addition to the O side of CO). The blue lines denote the long-range expansion given as the sum of the charge−dipole, charge−quadrupole, and charge−induced-dipole interactions. The red lines denote QCISD(T)/CBS calculations.

The rate coefficients for capture calculated for the QCISD(T)/CBS and three term long-range potential are essentially identical over the 10 to 400 K temperature range, with only a minor difference of 5% arising at the highest temperatures. This slight increase toward higher temperature is indicative of contributions from additional terms in the potential.

Near 10 K, the capture rate coefficients are of similar magnitude for all three terms in the potential. The charge−dipole and charge−quadrupole rate coefficients are proportional to $T^{-1/2}$ and $T^{-1/6}$, respectively, whereas the charge−induced-dipole capture is temperature independent. Thus, as the temperature rises, they both become small relative to the charge−induced-dipole rate coefficient. For the charge−quadrupole term, this decrease is quite gradual. As a result, the overall capture is not well-described by any single term for the full range of temperatures of interest here.

The long-range transition state theory approach employed in the preceding analysis typically overestimates the rate coefficient for capture by 5−10%.[27] This minor overestimate is corrected for here via trajectory simulations employing the three term long-range expansion. The good agreement between the TST
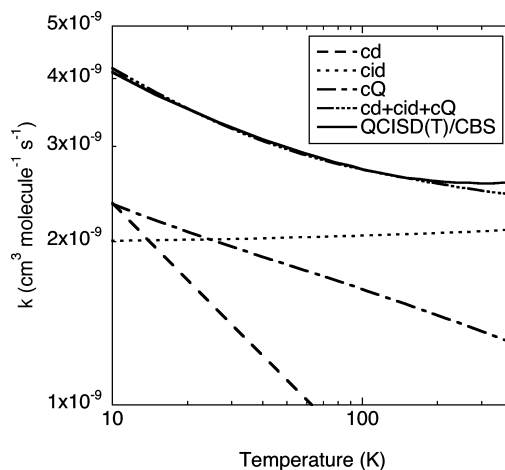

Figure 7. Temperature dependence of the calculated capture rate coefficient for CO + H_3^+ with the charge−dipole (dashed), charge−induced-dipole (dotted), charge−quadrupole (dashed-dotted), charge−dipole + charge−induced-dipole + charge−quadrupole (dash-dot-dot-dot), and the QCISD(T)/CBS ab initio potential (solid).

calculations of the capture rate coefficient for this potential and for the QCISD(T)/CBS potential implies that such long-range potential based trajectory simulations should be accurate. These simulations predict a dynamical correction factor of 0.90 ± 0.02 independent of temperature over the 10 to 400 K range. Our final predictions presented below include this dynamical correction factor.

The long-range interactions considered here are independent of the orientation of the H_3^+ ion. Correspondingly, the orientational average over the H_3^+ rotational degrees of freedom should have no effect on the predicted rate coefficient for capture. Importantly, this also suggests that the quantized nature of the H_3^+ rotational states, such as the separation into ortho and para states, should have little effect on the predicted rate coefficient for capture. Instead, quantum effects should only be significant at temperatures where they are important for the CO rotational partition function, which is about 5 K and lower.

The potential energy surface for the reaction of CO with H_3^+ was studied by Herbst and Woon[24] with high level CCSD(T)/aug-cc-pVTZ (coupled cluster with singles, doubles, and perturbative treatment of connected triples)[49] calculations. LeRoy and co-workers have recently obtained similar results (within 1 kcal/mol for the key stationary points) with larger basis sets and including core−valence correlation but employing the CCSD rather than CCSD(T) method in the geometry optimizations.[25] The addition leads to two distinct intermediate complexes, with the chemical bonding to either the O or the C end of the CO. These two intermediates lead to separate sets of bimolecular products, $H_2 + HCO^+$ and $H_2 + HOC^+$. A schematic diagram illustrating the reaction pathways for these reactions is provided in Figure 8. The rovibrational properties of the stationary points in this diagram were obtained at the QCISD(T)/aug-cc-pVTZ level. Higher level estimates for the energies were obtained from basis set extrapolations of QCISD(T) calculations with aug-cc-pVTZ and aug-cc-pVQZ basis sets. These energies are essentially identical to those of Herbst and Woon whose focus was instead on the kinetics of the $H_2 + HOC^+$ reaction.

These rovibrational properties were incorporated in transition state theory based master equation simulations of the rate coefficients for the two product channels. This analysis includes a treatment of the initial branching between the two addition complexes, the isomerization between the two complexes, and
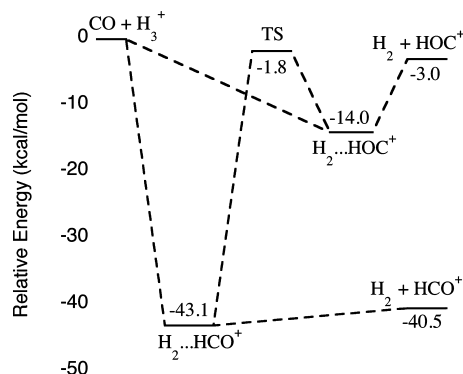
Figure 8. Schematic diagram of the stationary points on the potential energy surface for CO reacting with H_3^+. Energies are in kcal/mol relative to $CO + H_3^+$ and include zero-point corrections. They are obtained from QCISD(T)/CBS//QCISD(T)/aug-cc-pVTZ calculations.

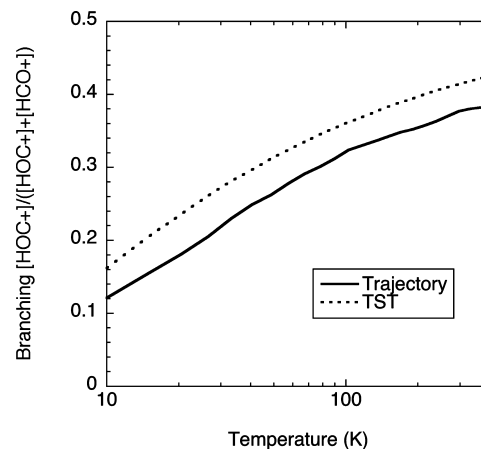**Figure 9.** Dependence of the branching fraction to $HOC^+ + H_2$ on temperature from trajectory simulations (solid) and from TST simulations (dotted).
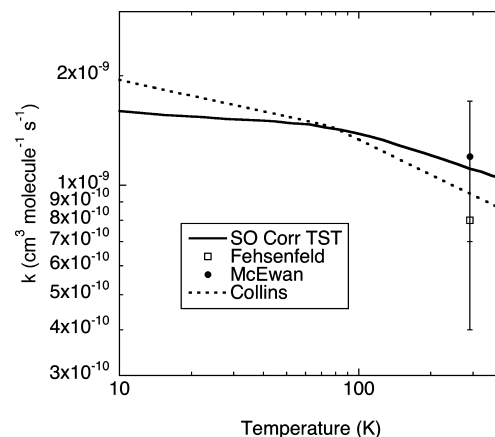

Figure 10. Plot of the rate coefficient for $O(^3P) + H_3^+$ as a function of temperature. The solid line denotes the present calculations based on the spin−orbit corrected CASPT2/CBS potentials (eq 11). The symbols denote the experiments from refs 18 and 19. The dotted line denotes the trajectory results from ref 21.

the dissociation of these complexes on to products and back to reactants. The rate constant for isomerization between the two complexes is obtained from rigid-rotor harmonic oscillator transition state theory and includes asymmetric Eckart tunneling corrections. The rate coefficients for decomposition to the two products are treated with long-range transition state theory. These transition state theory based evaluations were performed at the total energy, *E,* and total angular momentum, *J,* resolved level. We consider only the collisionless limit in this analysis because of our focus on interstellar chemistry, where the pressures are very low.

The branching in the initial addition was determined from both TST and trajectory simulations, with both approaches employing the three term long-range expansion of the potential. The perpendicular orientation of the CO moiety with respect to the center-of-mass to center-of-mass axis is predominantly repulsive. The assumption of an infinite barrier for this orientation then allows for separate TST estimates of the channel specific addition rate coefficients. Alternatively, the trajectory approach described in ref 34 provides the reactive flux for transitions between any pair of the three species $H_2...HCO^+$, $H_2...HOC^+$, and $CO + H_3^+$. Again, the perpendicular orientation of the CO is used to define a plane separating the $H_2...HCO^+$ and $H_2...HOC^+$ complexes.

These two predictions for the branching in the initial addition to the two complexes are illustrated in Figure 9. The two predictions are fairly similar but with the trajectory simulations yielding a few percent less $H_2...HOC^+$. At long-range, the charge−dipole term leads to a strong preference for the $H_2...HCO^+$ channel. This preference decreases with decreasing separation as the charge−quadrupole and charge−induced-dipole terms become more important. However, some memory of this preference as the reactants come together would yield a modest increase in the $H_2...HCO^+$ branching over the TST predictions as observed in Figure 9. The final master equation simulations employ the trajectory based estimates for this branching.

Results and Discussion

$O(^3P) + H_3^+$ Reaction. The present transition state theory based prediction for the temperature dependent capture rate coefficient for $O(^3P) + H_3^+$ is illustrated in Figure 10. The predicted room temperature rate coefficient of 1.1×10^{-9} cm^3 molecule^{-1} s^{-1} is in good agreement with the recent measurement of Milligan and McEwan[19] $((1.2 \pm 0.5) \times 10^{-9}$ cm^3

molecule^{-1} s^{-1}) and within the error bars of the earlier measurement of Fehsenfeld[18] $((0.8 \pm 0.4) \times 10^{-9}$ cm^3 mol-ecule^{-1} s^{-1}). The predicted rate coefficient is well-reproduced by the expression $1.14 \times 10^{-9} (T/300)^{-0.156} \exp(-1.41/T)$ cm^3 molecule^{-1} s^{-1} over the 5 to 400 K temperature range.

For most ion−molecule reactions, at least near room temperature, the rate coefficient for capture is largely determined by the charge−induced-dipole interaction. However, for this reaction, the capture rate coefficient is instead largely determined by the charge−quadrupole interaction for the full 5 to 400 K temperature range of interest here. This difference in behavior is due to the fact that for an atomic reactant the charge−quadrupole interaction is isotropic, whereas for a molecular reactant, the interaction is highly anisotropic with similar magnitude attractions and repulsions.

The rate coefficient is predicted to increase by a factor of 1.4 for a decrease in temperature from 300 to 30 K. This predicted rise with decreasing temperature is due to the fact that (i) the classical charge−quadrupole capture rate coefficient has a $T^{-1/6}$ temperature dependence and (ii) the electronic partition function for $O(^3P)$ decreases with decreasing temperature. The transition from the small *A* case to the large *A* case has the opposite effect of a decrease with decreasing *T* but is outweighed by the first two factors. The net result is that the predicted rate coefficient at 30 K of 1.5×10^{-9} cm^3 molecule^{-1}

s^{-1} is now comparable to the value of 1.7×10^{-9} cm^3 molecule^{-1} s^{-1} that has been commonly employed for the CO + H_3^+ reaction.

In making these predictions, we have assumed that the spin−orbit levels of O(^{3}P) are thermalized. As discussed by Goicoechea et al.,[50] in dense cloud conditions, this is not really the case for densities below the critical densities of the fine structure transition, (e.g., 5×10^5 cm^{-3} for $^3P_1-^3P_2$), and the fine structure excitation is a "complex non-local thermal equilibrium problem". But, for the low temperatures of the clouds considered here, the assumption of local thermal equilibrium is probably not too far off. Also, under the electronically adiabatic assumption, the $^3P_1$ and $^3P_0$ states are nonreactive, and so modest deviations in their populations from thermal equilibrium should not have a major effect on the predicted rate coefficients. The present calculations also yield rate coefficients for specific O(^{3}P) states. The adiabatic assumption implies that those for the $^3P_0$ and $^3P_1$ states are zero, while that for the $^3P_2$ state may be obtained from the thermal rate coefficient via multiplication by 1/5 of the temperature dependent electronic partition function for O(^{3}P) (i.e., $(5 + 3 \exp(-E(^3P_1)/k_BT) + \exp(-E(^3P_0)/k_BT))/5$).

The reaction of O(^{3}P) with H_3^+ has also been the subject of a detailed theoretical study by Collins and co-workers.[21] Their analysis was based on the propagation of classical trajectories on a potential obtained from fits to a set of MP2/6-311+G(2d,p) calculations. These authors consider the effect of the spin−orbit interaction on the electronic partition function of the O atom but do not consider its coupling to the charge−quadrupole interaction. Thus, their results, which are illustrated in Figure 10, roughly correspond to the present small *A* results plotted in Figure 4. Minor differences in the ab initio methods used and in the potential energy surface fitting contribute to the modest differences from our small *A* results. The present basis set extrapolation procedure and analytic long-range potential expansions are both expected to yield more accurate interaction energies. We would expect the present predictions to be accurate to about 10 to 20% over the 10 to 300 K temperature range.

Notably, as demonstrated in ref 21, the products H_2 + OH$^+$ and H + H_2O^+ are both highly exothermic. Furthermore, the H_2 + OH$^+$ channel leads barrierlessly to the OH_3^+ complex. Thus, the overall reaction rate coefficient for the O(^{3}P) + H_3^+ reaction is expected to be simply the capture rate coefficient that was calculated here. The study of ref 21 provides a useful indication of the branching ratio between the two exothermic channels.

CO + H_3^+ Reaction. The present transition state theory based rate coefficients for the reaction of CO with H_3^+ are illustrated in Figure 11. Over the 10 to 400 K temperature range, the predicted rate coefficient for the formation of H_2 + HCO$^+$ is well-reproduced by the modified Arrhenius expression 1.36×10^{-9} $(T/300)^{-0.142}$ $\exp(3.41/T)$ cm^3 molecule^{-1} s^{-1}, while that for the formation of H_2 + HOC$^+$ is well-reproduced by the expression 8.49×10^{-10} $(T/300)^{0.0661}$ $\exp(-5.21/T)$ cm^3 molecule^{-1} s^{-1}. Over this temperature range, the charge−dipole, the charge−quadrupole, and the charge−induced-dipole interactions are each important factors in the rate coefficient for capture. At low temperatures, the charge−dipole interaction is the most important, while at high temperatures the charge−induced-dipole interaction is the dominant factor. The charge−quadrupole interaction is significant throughout the 10 to 400 K range.

The dominant products are predicted to be H_2 + HCO$^+$. The initial addition rate coefficients are the sole determining factor in the branching ratio because the decomposition of H_2...HOC$^+$

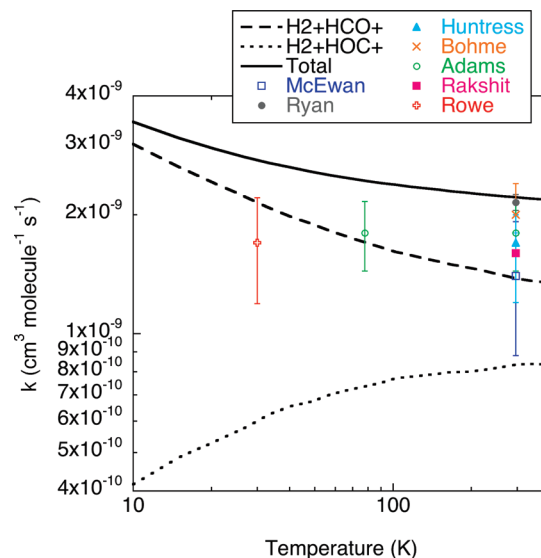**Figure 11.** Plot of the rate coefficient for CO + H_3^+ as a function of temperature. The dash, dot, and solid lines denote the present theoretical predictions for formation of H_2 + HCO$^+$, H_2 + HOC$^+$, and the total products, respectively. The symbols denote the experimental results from refs 15 and 51−57.

into H_2 + HOC$^+$ is much more rapid than the isomerization to H_2...HCO$^+$. This statement remains true even for changes of as much as ±1 kcal/mol in either the isomerization barrier or the H_2 + HOC$^+$ exothermicity. Such changes are at the limit of the uncertainties in these energies.

The branching to H_2 + HOC$^+$ decreases with decreasing temperature because the charge−dipole interaction is attractive for the approach of the C end of CO and repulsive for the O end. In the low temperature limit, the charge−dipole interaction is the dominant term in the potential. As the temperature rises, the charge−induced-dipole and charge−quadrupole terms both become larger in the transition state region than the charge−dipole interaction, and the two products are formed with similar rate coefficients.

Also plotted in Figure 11 are the various experimental measurements of the overall rate coefficient.[15,51−57] The theoretical prediction is in reasonable agreement with the room temperature experimental measurements, being at the upper end of the error bars for most of the more precise measurements. However, it is hard to understand the discrepancy with the one low temperature measurement of Rowe and co-workers.[57] With this discrepancy, a review of the factors causing the predicted temperature dependence and the uncertainties in the predictions seems warranted.

First, we note that the increase in the predicted rate coefficient with decreasing temperature is due to the increasing contributions of the charge−quadrupole and charge−dipole interactions, which have temperature dependences of $T^{-1/6}$ and $T^{-1/2}$, respectively. For this reason, it is important to use accurate electrostatic moments in the analysis. For example, if we had used the MP2/CBS dipole moment in place of the experimental dipole moment, then our predictions for the total rate coefficient would have been a factor of 1.3 larger at 30 K. Meanwhile, at this same temperature, the channel specific rate coefficient to form H_2 + HCO$^+$ would have been a factor of 1.4 larger, and that to form H_2 + HOC$^+$ would have been a factor of 3 lower. Clearly, the predicted branching ratio is extraordinarily sensitive to the dipole moment. Our use of the experimental moments and the good agreement between the direct QCISD(T)/CBS and three term analytic expansion implies that our underlying

potential is of high accuracy. Furthermore, the classical trajectory approach generally provides accurate capture rate coefficients down to quite low temperature. In this case, the classical capture rate coefficient should be accurate down to, at least, the rotational temperature of CO ($hcB/k_B = 2.8$ K) because the long-range interactions are independent of the H_3^+ orientation.

It is interesting to note that the channel specific rate coefficient for the production of $H_2 + HCO^+$ is in better agreement with the low temperature results than is the total rate coefficient. Thus, an error in the treatment of the decomposition of the $H_2...HOC^+$ adduct to $H_2 + HOC^+$ could remove the discrepancy. For example, an error in the predicted exothermicity for this channel could decrease the effective rate coefficient for its formation. However, as noted above, a reduction in this exothermicity by its maximum estimated uncertainty of 1 kcal/mol has a negligible effect on the predicted rate coefficients for CO + H_3^+. Furthermore, comparisons of theory and experiment (with either the present methods or as described in prior studies[24,26,58]) for the $H_2 + HOC^+$ rate coefficient suggest that the isomerization barrier should be lowered by about 1 kcal/mol. This lowering has essentially no effect on either the rate coefficient or branching fraction for the reaction of CO with H_3^+. Nevertheless, it should be noted that it is difficult to obtain quantitative agreement with the experimental data for the $H_2 + HOC^+$ rate coefficient with reasonable adjustments in the potential energy surface, especially for the high temperature data of ref 26. This difficulty may suggest that there are important quantum and/or dynamical effects that are mistreated in the present master equation based treatment.

In the absence of some important unforeseen effect, we expect the present theoretical predictions to be accurate to about 10−20%.

Astronomical Implications. In dense interstellar clouds, H_3^+ is produced by cosmic rays at a rate of $\zeta n(H_2)$, where ζ is the cosmic-ray ionization rate (typically adopted to be $\sim 3 \times 10^{-17}$ s^{-1}) and $n(H_2)$ is the number density of molecular hydrogen (typically of order $10^4 - 10^6$ cm^{-3}). If, as in McCall et al.,[12] proton transfer to CO is considered to be the dominant destruction mechanism, H_3^+ will be destroyed at a rate of $k_{CO}n(H_3^+)n(CO)$. In steady state, these rates can be equated and solved for the H_3^+ number density to yield $n(H_3^+) = (\zeta n(H_2))/(k_{CO}n(CO))$. Since column densities rather than number densities are the observable quantities, it is more convenient to transform this expression by using the relationship $N(H_3^+) \sim n(H_3^+)\cdot L$, where $N(H_3^+)$ is the observed column density of H_3^+ in a particular cloud and L is the absorption path length through that cloud. This relationship is a very good approximation because $n(H_3^+)$ does not directly depend on cloud density but only on ζ and the H_2/CO ratio. The former is assumed to be constant because of the long penetration depth of ~ 100 MeV cosmic rays, and the latter is constant because essentially all hydrogen is in the form H_2 and essentially all carbon is in the form CO. With this substitution, we can express the product of the unknown quantities ζ and L in terms of known quantities:

$$\zeta L = N(H_3^+)\cdot[k_{CO}n(CO)]/n(H_2) \qquad (15)$$

The quantity in square brackets represents the destruction rate for an individual H_3^+ molecule in a dense cloud, and in light of the present results, this should be modified to include the effect of O atoms. A more complete expression would be $[k_{CO}n(CO) + k_On(O)]$, but this can be somewhat simplified. The cosmic abundance of oxygen is roughly twice that of carbon, and
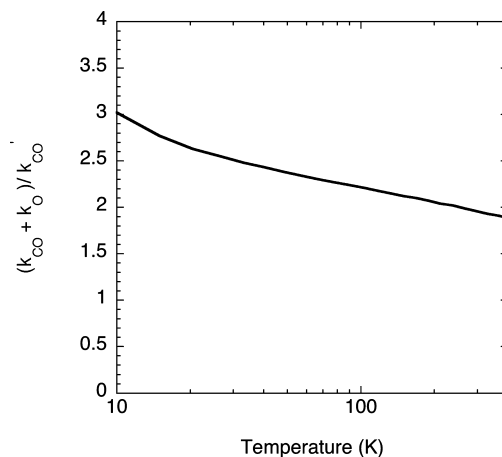

Figure 12. Plot of the temperature dependence of the predicted increase in the destruction rate of H_3^+, $(k_{CO} + k_O)/k_{CO'}$, compared with the analysis of McCall et al.[12]

essentially every carbon atom soaks up an equivalent of oxygen in producing CO. Assuming that all of the remaining oxygen atoms are not chemically bound, it is a good approximation to say that $n(O) \sim n(CO)$. Consequently, we can express the H_3^+ destruction rate as $\sim[k_{CO} + k_O]n(CO)$. If we denote the "old" value of k_{CO} (1.7×10^{-9} cm^3 molecule^{-1} s^{-1}) as $k_{CO'}$, then the destruction rate of H_3^+ should be increased, compared with the analysis of McCall et al.,[12] by a factor of $(k_{CO} + k_O)/k_{CO'}$. This quantity is plotted as a function of temperature in Figure 12, and at the temperatures typical of dense clouds (10−30 K), it is 2.5 to 3.0.

As evident from eq 15, this increased destruction rate translates directly to an increase in either the cosmic-ray ionization rate ζ or the cloud path length L. Future observations and analyses to better constrain the cloud density (and thereby the path length) in sightlines where H_3^+ has been observed would therefore be highly desirable, as they could break this degeneracy between ζ and L.

In addition to the direct impact on H_3^+, the higher rate coefficient for the $H_3^+ + O$ reaction also suggests that interstellar water will be produced more quickly than previously thought. This reaction produces either OH^+ or H_2O^+, both of which can undergo hydrogen abstraction reactions with abundant H_2 to form H_3O^+. The latter ion can dissociatively recombine with electrons to form either H_2O or OH; the branching ratio for this recombination has been somewhat controversial, with storage ring measurements[59,60] indicating a modest ($\sim 25\%$) branching fraction to H_2O but flowing afterglow studies[61] suggesting a much lower ($\sim 5\%$) branching fraction. Regardless of the correct branching ratio, increasing the rate of the $H_3^+ + O$ reaction will speed up the production of interstellar water. The abundance of interstellar water is a matter of great interest in terms of both astrochemistry and astrobiology and is the subject of a Key Programme of the recently launched Herschel Space Observatory.

Finally, we wish to emphasize the surprising result that the $H_3^+ + CO$ reaction forms an appreciable fraction of HOC^+, as indicated in Figure 11. The branching fraction to HOC^+ has traditionally been assumed to be 6 ± 5%, on the basis of collision induced dissociation experiments.[62] However, as emphasized by DeFrees et al.,[58] these experiments are complex and somewhat indirect. The relatively low observed HCO^+/HOC^+ ratios of $\sim 360-6000$ observed in molecular clouds[63] have been somewhat difficult to reconcile with the high rate coefficient ($\sim 4 \times 10^{-10}$ cm^3 molecule^{-1} s^{-1}) for the isomer-

T Dependence of Two Key Interstellar Reactions

J. Phys. Chem. A, Vol. 114, No. 1, 2010 **287**

ization reaction $HOC^+ + H_2 \rightarrow HCO^+ + H_2$ observed in a cold ion trap.[64] Perhaps the higher branching fraction of HOC^+ formation indicated in the present calculations can help resolve this discrepancy.

The arguments presented here regarding the impact of the newly calculated reaction rates are based on a very simplistic analysis, assuming steady state and considering only a limited number of reactions. To fully explore the ramifications of these results on astrochemistry, it will be necessary to perform more detailed, time-dependent calculations using a full chemical network. In certain cases, dependencies in such complex networks can reduce the effects on molecular abundances that result from changing individual rate coefficients. Preliminary results from such chemical models indicate that in this case, our simple arguments are at least qualitatively correct.[65]

Conclusion

The present theoretical analysis predicts that for both the $O(^3P) + H_3^+$ and the $CO + H_3^+$ reactions the rate coefficient increases significantly with decreasing temperature. As a result, the destruction rate for H_3^+ in dense clouds is predicted to be 2.5 to 3 times greater than assumed in the model of McCall et al.[12] For the $O(^3P)$ reaction, there are no experimental studies of the temperature dependence. For the CO reaction experiment suggests that the rate coefficient should be independent of temperature.[55] Given the importance of the predicted revision to the destruction rate, additional low temperature studies of these reactions are needed to confirm the predicted temperature dependence for the $O(^3P)$ reaction and/or to help resolve the discrepancy between theory and experiment for the CO reaction.

Appendix A

Quadrupole Moment of an Atom. In this appendix, we discuss the quadrupole moment Q for an atom with an open p shell. We start with a review of the general description for the quadrupole moment tensor. We then provide some simple qualitative results that show the effect of symmetry on the quadrupole moment for an atom.

The operator for the interaction of a quadrupole with an electric field is given by[66]

$$\hat{V}_{qQ} = \frac{1}{6}\frac{\partial^2 \phi}{\partial x_i \partial x_k}\hat{Q}_{ik} \quad (A1)$$

where φ is the electric field potential and $\hat{Q}_{ik}$ is the operator for the quadrupole moment of the system.

The quadrupole moment operator is a symmetric tensor of the second rank with zero trace. Because of its transformational properties, the most general form for such a tensor, $\hat{Q}_{ik}$, averaged over all degrees of freedom except the direction of the angular momentum is[67]

$$\hat{Q}_{ik} = \frac{3Q}{2J(2J-1)}\left(\hat{J}_i\hat{J}_k + \hat{J}_k\hat{J}_i - \frac{2}{3}J(J+1)\delta_{ik}\right) \quad (A2)$$

The normalization factor in eq A2 is chosen so that the constant Q, which uniquely defines the quadrupole moment operator, corresponds to the value of its z component, $\hat{Q}_{zz}$, in the $|M_J = J\rangle$ rotational state. This constant is commonly referred to as the quadrupole moment for an atom.

TABLE A1: Orbital Wave Functions and Quadrupole Moments, Q, for 1, 2, and 3 Electron p Shell Cases

shell	configuration	wave function	quadrupole moment
p^1	^2P	$|1\rangle$	Q_1
p^2	^3P	$(1/2)^{1/2}(|1\rangle|0\rangle - |0\rangle|1\rangle)$	$-Q_1$
	^1D	$|1\rangle|1\rangle$	$2Q_1$
p^3	^2P	$1/2(|1\rangle|0\rangle|0\rangle - |0\rangle|1\rangle|0\rangle - |1\rangle|-1\rangle|1\rangle + |-1\rangle|1\rangle|1\rangle)$	0
	^2D	$(1/2)^{1/2}(|1\rangle|1\rangle|0\rangle - |1\rangle|0\rangle|1\rangle)$	0

Note that substituting in eq 1 the potential of a point charge for an ion and expression (eq A2) for $\hat{Q}_{ik}$ in terms of the orbital angular momentum, $\hat{L}_i$, yields eq 2.

Standard electronic structure software packages provide routine procedures for evaluating the quadrupole moment Q in eq A2. Such procedures include the multireference nature of the wave function and as a result, although numerically accurate, are fairly complicated. It is instructive to consider the simpler derivation of expressions for Q for atoms with an open p shell within the Hartree−Fock approximation. These expressions demonstrate the effect of the symmetry of the atomic wave function on its quadrupole moment. While these expressions may not be very accurate due to the multireference nature of the wave function, they do provide order of magnitude estimates for the quadrupole moment. More importantly, in most cases, they provide the right sign of the quadrupole moment, which is crucial for the qualitative understanding of the structure of the energy levels. Note, however, that the actual calculations presented in the text employ the accurate expressions obtained from high-level electronic structure evaluations rather than these simple Hartree−Fock estimates.

Within the Hartree−Fock approximation, the quadrupole moment, Q_1, for a single p electron in an atom is given by[68]

$$Q_1 \equiv \langle 1|\hat{Q}_{zz}|1\rangle = \langle -1|\hat{Q}_{zz}|-1\rangle = \frac{2}{5}|e|\langle r^2\rangle \quad (A3)$$

$$\langle 0|\hat{Q}_{zz}|0\rangle = -2Q_1 \quad (A4)$$

where $\langle r^2\rangle$ is the average distance squared of the electron from the nucleus and the one-electron wave function in the state with the M_L orbital angular momentum projection is denoted as $|M_L\rangle$.

The corresponding quadrupole moments for the cases of 2 and 3 electrons (p^2 and p^3) are given in Table A1. The quadrupole moments for the cases of 4 and 5 electrons can be reduced to those for the p^2 and p^1 cases by viewing them as having 2 and 1 holes, respectively, with the quadrupole moment reversing its sign for the corresponding configurations. The results in the table show the orbital part of the wave function and the corresponding quadrupole moment (we do not consider S configurations, for which the quadrupole moment is, obviously, zero). Our results coincide with those of Gentry and Giese.[22]

Appendix B

Charge−Quadrupole Interaction with Spin−Orbit Coupling. In this appendix, we derive the expression for the electronic energy in the presence of the charge−quadrupole and spin−orbit interactions, eq 6. To find the eigenvalues of the Hamiltonian (6) one notes that, because of cylindrical symmetry, the z component of the total electronic angular momentum is conserved. Thus, the nine-dimensional (3 × 3) phase space of

the system is separated into the $M_J = 0$ three-dimensional subspace ($J = 0, 1, 2$) and two doubly degenerate $M_J = \pm1$ two-dimensional ($J = 1,2$) and $M_J = \pm2$ one-dimensional ($J = 2$) subspaces. Further simplification arises from the observation that the Hamiltonian (6) is also invariant under rotation about the *x* axis by 180°. As a result, the $M_J = 0$ three-dimensional subspace is naturally subdivided into the two-dimensional ($J = 0, 2$) subspace, whose elements are invariant under this rotation and the one-dimensional $J = 1$ subspace whose vectors change sign under it.

To calculate the matrix elements of the Hamiltonian (6), we will use the eigenstates of the total electronic angular momentum and its *z* component as a basis, in which the spin−orbit coupling operator is diagonal. To calculate the matrix elements of the quadrupole term in the Hamiltonian (6), we will explicitly express the eigenstates of the total electronic angular momentum in terms of the $|M_L, M_S\rangle$ states.

$M_J = 0$, $J = 0,2$ Subspace. The eigenstates of the total electronic angular momentum are given by

$$|J = 0, M_J = 0\rangle = \sqrt{1/3}(|0, 0\rangle - |1, -1\rangle - |-1, 1\rangle)$$
(B1)

and

$$|J = 2, M_J = 0\rangle = \sqrt{1/6}(2|0, 0\rangle + |1, -1\rangle + |-1, 1\rangle)$$
(B2)

which can be checked directly by application of the ascending and descending ladder operators $\hat{J}_+$ and $\hat{J}_-$ to them. Using these equations, one obtains the following expressions for the matrix elements of the $\hat{L}_z^2$ operator, (we omit the $M_J = 0$ index for simplicity of notation)

$$\langle 0|\hat{L}_z^2|0\rangle = 2/3, \langle 2|\hat{L}_z^2|2\rangle = 1/3, \langle 0|\hat{L}_z^2|2\rangle = -\sqrt{2}/3$$
(B3)

and the Hamiltonian matrix in this subspace is given by

$$\begin{pmatrix} 2A & -B\sqrt{2}/3 \\ -B\sqrt{2}/3 & -A - B/3 \end{pmatrix}$$
(B4)

The diagonal elements of this matrix provide the (approximate) energies in the corresponding *J* states ($2A$ for the $|J = 0\rangle$ state and $-A - B/3$ for the $|J = 2\rangle$ state) in the strong spin−orbit coupling limit (low temperatures, large interfragment separations). The eigenvalues of this Hamiltonian are given by

$$E_{1,2} = A/2 - B/6 \pm \sqrt{\frac{9}{4}A^2 + \frac{AB}{2} + \frac{B^2}{4}}$$
(B5)

The first eigenstate (with the plus sign in front of the square root term in this equation) correlates with one of six degenerate repulsive states at small separations, where the charge−quadrupole interaction dominates, eq 3. At large separations, when spin−orbit coupling is the dominant interaction, it correlates with the $|J = 0\rangle$ spin−orbit state. The second eigenstate correlates with one of the triply degenerate attractive states at small separations, eq 3, and with one of the quintuply degenerate $|J = 2\rangle$ spin−orbit states at large separations.

TABLE A2: Energy Levels in the Strong Spin−Orbit Coupling Limit

J	E_{LS}	M_J	E_{qQ}
2	$-A$	2	$B/3$
		1	$-B/6$
		0	$-B/3$
1	A	1	$-B/6$
		0	$B/3$
0	$2A$	0	0

TABLE A3: *J* Dependence of Effective Quadrupole Moment for the Strong Spin−Orbit Coupling Case

J	$|J, M_J = J\rangle$	Q_J
2	$|1,1\rangle$	Q
1	$(1/2)^{1/2}(|1,0\rangle - |0,1\rangle)$	$-Q/2$

$M_J = 0$, $J = 1$ Subspace. The eigenstate of the total electronic angular momentum is given by

$$|J = 1, M_J = 0\rangle = \sqrt{1/2}(|1, -1\rangle - |-1, 1\rangle)$$
(B6)

the matrix element of $\hat{L}_z^2$ is given by

$$\langle 1|\hat{L}_z^2|1\rangle = 1$$
(B7)

and the energy of this state is given by

$$E = A + B/3$$
(B8)

At small separations, it correlates with one of the six degenerate repulsive states, eq 3. At large separations, this state correlates with one of the triply degenerate $|J = 1\rangle$ spin−orbit states.

$M_J = 1$, $J = 1, 2$ Subspace. The eigenstates of the total electronic angular momentum are given by

$$|J = 1, M_J = 1\rangle = \sqrt{1/2}(|1, 0\rangle - |0, 1\rangle)$$
(B9)

and

$$|J = 2, M_J = 1\rangle = \sqrt{1/2}(|1, 0\rangle + |0, 1\rangle)$$
(B10)

Then the matrix elements of $\hat{L}_z^2$ are given by

$$\langle 1|\hat{L}_z^2|1\rangle = 1/2, \langle 2|\hat{L}_z^2|2\rangle = 1/2, \langle 1|\hat{L}_z^2|2\rangle = 1/2$$
(B11)

and the Hamiltonian matrix is given by

$$\begin{pmatrix} A - B/6 & B/2 \\ B/2 & -A - B/6 \end{pmatrix}$$
(B12)

The diagonal elements of this matrix provide the (approximate) energies for the corresponding *J* states ($A - B/6$ for the $|J = 1\rangle$ state and $-A - B/6$ for the $|J = 2\rangle$ state) in the strong spin−orbit coupling limit (low temperature, large separation). The eigenvalues of this Hamiltonian are given by

$$E_{1,2} = -B/6 \pm \sqrt{A^2 + B^2/4} \qquad \text{(B13)}$$

The first eigenstate (with the plus sign in front of the square root term in this equation) correlates with one of the six degenerate repulsive states at small separations, eq 3, when the charge−quadrupole interaction dominates. At large separations, when spin−orbit coupling is a dominant interaction, it correlates with one of the triply degenerate $|J = 1\rangle$ spin−orbit states. The second eigenstate correlates with one of the three degenerate attractive states at small separations, eq 3. At large separations, it correlates with one of the quintuply degenerate $|J = 2\rangle$ spin−orbit states.

$M_J = 2, J = 2$ *Subspace.* The eigenstate of the total electronic angular momentum is given by

$$|J = 2, M_J = 2\rangle = |1, 1\rangle \qquad \text{(B14)}$$

the matrix element of $\hat{L}_z^2$ is given by

$$\langle 1|\hat{L}_z^2|1\rangle = 1 \qquad \text{(B15)}$$

and the energy of this state is given by

$$E = -A + B/3. \qquad \text{(B16)}$$

At small separations, it correlates with one of the six degenerate repulsive states, eq 3. At large separations, this state correlates with one of the quintuply degenerate $|J = 2\rangle$ spin−orbit states.

In the strong spin−orbit coupling limit (large interfragment separation), the preceding results for the (approximate) energies are summarized in Table A2. These expressions can be obtained more easily by noting that in the strong spin−orbit coupling limit the total electronic angular momentum J is a good quantum number. In this case, the operator for the quadrupole tensor is expressed by eq A2 with the operator for the total electronic angular momentum, $\hat{J}_i$, used instead of the orbital one.[69] The effective quadrupole moment Q_J then depends on the value of J. Its values are presented in Table A3 together with the corresponding wave function $|J, M_J = J\rangle$ in the $|M_L, M_S\rangle$ representation for each J.

References and Notes

(1) Geballe, T. R.; Oka, T. *Nature* **1996**, *384*, 334.
(2) McCall, B. J.; Geballe, T. R.; Hinkle, K. H.; Oka, T. *Science* **1998**, *279*, 1910.
(3) McCall, B. J.; Hinkle, K. H.; Geballe, T. R.; Moriarty-Schieven, G. H.; Evans, N. J., II.; Kawaguchi, K.; Takano, S.; Smith, V. V.; Oka, T. *Astrophys. J.* **2002**, *567*, 391.
(4) McCall, B. J.; Huneycutt, A. J.; Saykally, R. J.; Geballe, T. R.; Djuric, N.; Dunn, G. H.; Semaniak, J.; Novotny, O.; Al-Khalili, A.; Ehlerding, A.; Hellberg, F.; Kalhori, S.; Neau, A.; Thomas, R.; Osterdahl, F.; Larsson, M. *Nature* **2003**, *422*, 500.
(5) Kreckel, H.; Motsch, M.; Mikosch, J.; Glosik, J.; Plasil, R.; Altevogt, S.; Andrianarijaona, V.; Buhr, H.; Hoffmann, J.; Lammich, L.; Lestinsky, M.; Nevo, I.; Novotny, S.; Orlov, D. A.; Pedersen, H. B.; Sprenger, F.; Terekhov, A. S.; Toker, J.; Wesler, R.; Gerlich, D.; Schwalm, D.; Wolf, A.; Zajfman, D. *Phys. Rev. Lett.* **2005**, *95*, 3201.
(6) Kokoouline, V.; Greene, C. H. *Phys. Rev. Lett.* **2003**, *90*, 133201.
(7) Kokoouline, V.; Greene, C. H. *Phys. Rev. A* **2003**, *68*, 012703.
(8) Indriolo, N.; Geballe, T. R.; Oka, T.; McCall, B. J. *Astrophys. J.* **2007**, *671*, 1736.
(9) Dalgarno, A. *Proc. Natl. Acad. Sci.* **2006**, *103*, 12269.
(10) Indriolo, N.; Fields, B. D.; McCall, B. J. *Astrophys. J.* **2009**, *694*, 257.
(11) Lovas F. J., Snyder L. E. In *CRC Handbook of Chemistry and Physics*, 85th ed.; Lide, D. R., Jr., Ed.; CRC: Boca Raton, FL; 2005; pp 6−8, Section 14.
(12) McCall, B. J.; Geballe, T. R.; Hinkle, K. H.; Oka, T. *Astrophys. J.* **1999**, *522*, 338.
(13) Kulesa, C. Ph. D. Thesis, 2002, University of Arizona.
(14) Brittain, S. D.; Simon, T.; Kulesa, C.; Rettig, T. W. *Astrophys. J.* **2004**, *606*, 911.
(15) Kim, J. K.; Theard, L. P.; Huntress, W. T. *Chem. Phys. Lett.* **1975**, *32*, 610.
(16) Buhl, D.; Snyder, L. E. *Nature* **1970**, *228*, 267.
(17) Lee, H.-H.; Bettens, R. P. A.; Herbst, E. *Astron. Astrophys. Suppl.* **1996**, *119*, 111.
(18) Fehsenfeld, F. C. *Astrophys. J.* **1976**, *209*, 638.
(19) Milligan, D. B.; McEwan, M. J. *Chem. Phys. Lett.* **2000**, *319*, 482.
(20) Wakelam, V.; Loison, J.-C.; Herbst, E.; Talbi, D.; Quan, D.; Caralp, F. *Astron. Astrophys.* **2009**, *495*, 513.
(21) Bettens, R. P. A.; Hansen, T. A.; Collins, M. A. *J. Chem. Phys.* **1999**, *111*, 6322.
(22) Gentry, W. R.; Giese, C. F. *J. Chem. Phys.* **1977**, *67*, 2355.
(23) Talbi, D.; DeFrees, D. J.; Egolf, D. A.; Herbst, E. *Astrophys. J.* **1991**, *374*, 390.
(24) Herbst, E.; Woon, D. E. *Astrophys. J.* **1996**, *463*, L113.
(25) Li, H.; Hirano, T.; Amano, T.; LeRoy, R. J. *J. Chem. Phys.* **2008**, *129*, 244306.
(26) Jarrold, M. F.; Bowers, M. T.; DeFrees, D. J.; McLean, A. D.; Herbst, E. *Astrophys. J.* **1986**, *303*, 392.
(27) Georgievskii, Y.; Klippenstein, S. J. *J. Chem. Phys.* **2005**, *122*, 194103.
(28) See, for example, references cited in Klippenstein, S. J. Georgievskii, Y. Theory of Low Temperature Gas Phase Reactions. *Low Temperatures and Cold Molecules*; Smith, I. W. M., Ed.; World Scientific: River Edge, NJ, 2008.
(29) Klippenstein, S. J. *J. Chem. Phys.* **1992**, *96*, 367.
(30) Georgievskii, Y.; Klippenstein, S. J. *J. Phys. Chem. A* **2003**, *107*, 9776.
(31) Klippenstein, S. J.; Harding, L. B. *Phys. Chem. Chem. Phys.* **2006**, *8*, 1133.
(32) Harding, L. B.; Georgievskii, Y.; Klippenstein, S. J. *J. Phys. Chem. A* **2005**, *109*, 4646.
(33) Klippenstein, S. J.; Georgievskii, Y.; Harding, L. B. *Proc. Comb. Inst.* **2002**, *29*, 1229.
(34) Harding, L. B.; Georgievskii, Y.; Klippenstein, S. J. *J. Phys. Chem. A*, 2009, submitted.
(35) Note that the charge quadrupole derivation of ref 27 is applicable only to the case of the interaction of a charge with a permanent quadrupole moment for a single electronic state as with a molecule. The present case of an atom with degenerate ground electronic states and spin−orbit interactions requires the more complicated analysis outlined here.
(36) Celani, P.; Werner, H.-J. *J. Chem. Phys.* **2000**, *112*, 5546−5557.
(37) Martin, J. M. L. *Chem. Phys. Lett.* **1996**, *259*, 669.
(38) Feller, D.; Dixon, D. A. *J. Chem. Phys.* **2001**, *115*, 3484.
(39) Greenwald, E. E.; North, S. W.; Georgievskii, Y.; Klippenstein, S. J. *J. Phys. Chem. A* **2005**, *109*, 6031.
(40) Dunning, T. H., Jr. *J. Chem. Phys.* **1989**, *90*, 1007.
(41) Kendall, R. A.; Dunning, T. H., Jr.; Harrison, R. J. *J. Chem. Phys.* **1992**, *96*, 6796.
(42) Pople, J. A.; Head-Gordon, M.; Raghavachari, K. *J. Chem. Phys.* **1987**, *87*, 5968.
(43) Werner, H.-J.; Knowles, P. J.; Almlof, J.; Amos, R. D.; Berning, A.; Cooper, D. L.; Deegan, M. J. O.; Dobbyn, A. J.; Eckert, F.; Elbert, S. T.; Hampel, C.; Lindh, R.; Lloyd, A. W.; Meyer, W.; Nicklass, A.; Peterson, K.; Pitzer, R.; Stone, A. J.; Taylor, P. R.; Mura, M. E.; Pulay, P.; Schutz, M.; Stoll, H.; Thorsteinsson, T. MOLPRO; 2006.1. ed., 2006.
(44) Alpher, R. A.; White, D. R. *Phys. Fluids* **1959**, *2*, 153.
(45) Muenter, J. S. *J. Mol. Spectrosc.* **1975**, *55*, 490.
(46) Maroulis, G. *Chem. Phys. Lett.* **2001**, *334*, 214.
(47) Bridge, N. J.; Buckingham, A. D. *Proc. R. Soc. London, Ser. A* **1966**, *295*, 334.
(48) Note that for the purposes of this comparison and the following rate comparison we have employed the QCISD(T)/CBS properties for the long-range terms rather than the experimental values.

(49) Raghavachari, K.; Trucks, G. W.; Pople, J. A.; Head-Gordon, M. *Chem. Phys. Lett.* **1989**, *157*, 479.

(50) Goicoechea, J. R.; Compiegne, M.; Habart, E. *Astrophys. J.* **2009**, *699*, L165.

(51) Burt, J. A.; Dunn, J. L.; McEwan, M. J.; Sutton, M. M.; Roche, A. E.; Schiff, H. I. *J. Chem. Phys.* **1970**, *52*, 6062.

(52) Ryan, K. R. *J. Chem. Phys.* **1974**, *61*, 1559.

(53) Tanner, S. D.; Mackay, G. I.; Hopkinson, A. C.; Bohme, D. K. *Int. J. Mass Spec. Ion Phys.* **1979**, *29*, 153.

(54) Bohme, D. K.; Mackay, G. I.; Schiff, H. I. *J. Chem. Phys.* **1980**, *73*, 4976.

(55) Adams, N. G.; Smith, D. *Astrophys. J.* **1981**, *248*, 373.

(56) Rakshit, A. B. *Int. J. Mass Spec. Ion Phys.* **1982**, *41*, 185.

(57) Marquette, J. B.; Rebrion, C.; Rowe, B. R. *Astron. Astrophys.* **1989**, *213*, L29.

(58) DeFrees, D. J.; McLean, A. D.; Herbst, E. *Astrophys. J.* **1984**, *279*, 322.

(59) Neau, A.; Al Khalili, A.; Rosen, S.; Le Padellec, A.; Derkach, A. M; Shi, W.; Vikor, L.; Larsson, M.; Semaniak, J.; Thomas, R.; Nagard, M. B.; Andersson, K.; Danared, H.; af Ugglas, M. *J. Chem. Phys.* **2000**, *113*, 1762.

(60) Jensen, M. J.; Bilodeau, R. C.; Safvan, C. P.; Seiersen, K.; Andersen, L. H.; Pedersen, H. B.; Heber, O. *Astrophys. J.* **2000**, *543*, 764.

(61) Williams, T. L.; Adams, N. G.; Babcock, L. M.; Herd, C. R.; Geoghegan, M. *Mon. Not. R. Astron. Soc.* **1996**, *282*, 413.

(62) Illies, A. J.; Jarrold, M. F.; Bowers, M. T. *J. Am. Chem. Soc.* **1983**, *105*, 2562.

(63) Apponi, A. J.; Ziurys, L. M. *Astrophys. J.* **1997**, *481*, 800.

(64) Smith, M. A.; Schlemmer, S.; von Richthofen, J.; Gerlich, D. *Astrophys. J.* **2002**, *578*, L87.

(65) Herbst, E. private communication, 2009.

(66) Landau, L. D.; Lifshitz, E. M. *The Classical Theory of Fields*; Pergamon Press: London, 1975.

(67) Landau, L. D.; Lifshitz, E. M. *Quantum Mechanics, Non-Relativistic Theory*; Pergamon Press: London, 1965; p 262.

(68) Reference 67, p 263, problem 2.

(69) Reference 67, p 262, problem 1.